buildings

MDPI

Article

Experimental Study on Vertical Bearing and Deformation Characteristics of Qiantang River Ancient Seawall

Qiang Chen [1], Xiaobin Tu [1], Yongcheng Lv [1], Wei Liu [2] and Li Shi [3,*]

[1] Huadong Engineering Corporation Limited, Hangzhou 310005, China; chen_q2@hdec.com (Q.C.); tu_xb@hdec.com (X.T.); lv_yc3@hdec.com (Y.L.)
[2] Harbor, Coastal and Offshore Engineering, Hohai University, Xikang Road Campus, Nanjing 210024, China; leo2507199130@outlook.com
[3] College of Civil Engineering, Zhejiang University of Technology, Pingfeng Campus, Hangzhou 310012, China
* Correspondence: lishi@zjut.edu.cn

Abstract: Situated on the northern bank of the Qiantang River estuary, the ancient seawall serves not only as a national cultural relic but also as an active agent in flood and tide prevention. This seawall features a trapezoidal cross-section and is constructed with layered stone blocks and a sticky rice mortar. To investigate the load-bearing and deformation attributes of this ancient structure, a scaled-down specimen with a ratio of 1:4 was created. Monotonic and cyclic vertical loadings were then applied to the wall's top surface. During these loading procedures, measurements of the loading force, seawall displacement, and front and side deformation fields were taken. Experimental findings reveal that the seawall tends to lean towards the soil-retaining side under vertical loading. After ten loading cycles, the vertical rigidity of the wall was reduced by 10%. Upon application of a uniformly distributed vertical load of 1.6 MPa at the top of the wall, significant cracks began to materialize in the blocks at the base of the seawall. When the loading at the top increased to 2 MPa, a vertical crack that cut through the mortar layer at the wall's center was observed. By comparing it to a three-dimensional finite element model, the load-bearing and deformation characteristics of the ancient seawall observed in the experiments were confirmed, which could contribute to the scientifically informed conservation and protection of the seawall.

Keywords: ancient seawall; stone masonry; bearing characteristics; quasi-static test; vertical rigidity

check for updates

Citation: Chen, Q.; Tu, X.; Lv, Y.; Liu, W.; Shi, L. Experimental Study on Vertical Bearing and Deformation Characteristics of Qiantang River Ancient Seawall. *Buildings* **2023**, *13*, 2788. https://doi.org/10.3390/buildings13112788

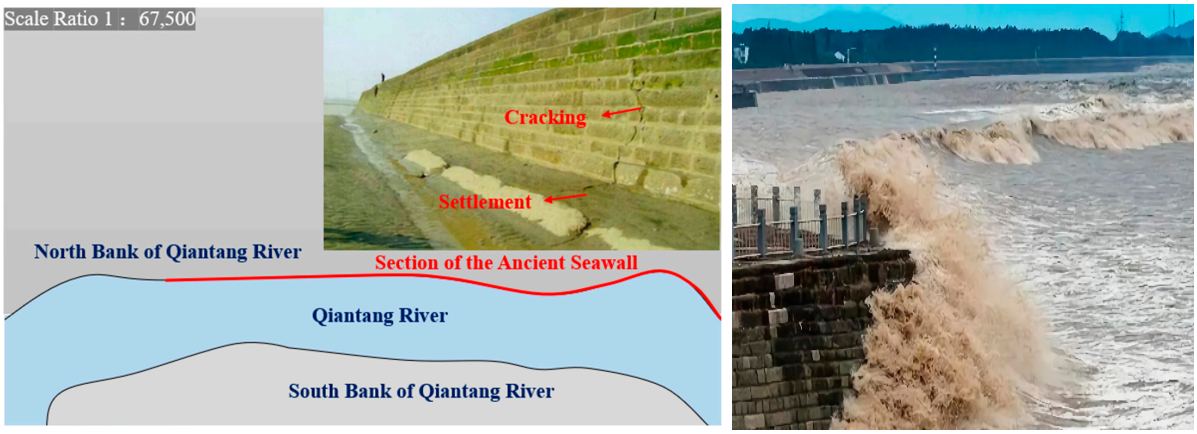
Academic Editor: Humberto Varum

Received: 5 September 2023
Revised: 28 October 2023
Accepted: 1 November 2023
Published: 6 November 2023

Copyright: © 2023 by the authors. Licensee MDPI, Basel, Switzerland. This article is an open access article distributed under the terms and conditions of the Creative Commons Attribution (CC BY) license (https://creativecommons.org/licenses/by/4.0/).

1. Introduction

The Qiantang River ancient seawall, situated on the northern bank of the Qiantang River estuary in Hangzhou, Zhejiang Province (Figure 1a), functions as both a national cultural relic and a flood and tide mitigator. Constructed during the Ming dynasty (i.e., about 14th century), this seawall comprises layered masonry of slab stones and sticky rice mortar. Its cross-section, which is trapezoidal, consists of 17 stone layers, each decreasing in width from bottom to top. The Qiantang River estuary belongs to the subtropical monsoon climate zone, which is characterized by distinct four seasons. The river estuary experiences an irregular, semi-diurnal tidal flow with two high and low tides per day. According to hydrology statistics, the multi-year average highest tidal level is 6.06 m; the average high tide level is 4.03 m; the average tidal level is 2.45 m. Owing to its unique trumpet-shaped estuary, the tide bore formed at the Qiantang River estuary is characterized by a high propagation speed (up to 6 m/s) and a large tidal bore height (up to 3.5 m) (Figure 1b). Subjected to the cyclic impact of the river's forceful tidal bore, the seawall has been destroyed and rebuilt about 20 times in its long history from the 14th to 20th centuries (i.e., covering the Ming and Qing dynasty of China) since its construction, which indicates that the estimated return period for this construction is around 35 years.



(**a**) (**b**)

Figure 1. Qiantang River ancient seawall: (**a**) Qiantang River estuary and ancient seawall; (**b**) surging tide impacting the ancient seawall.

Currently, the seawall has shown structural vulnerabilities, such as cracking in the seawall body and erosion of the foundation (Figure 1a). These damages threaten the structural safety and load-bearing stability of the cultural relic. Thus, it is essential to conduct experimental investigations on the seawall's load-bearing and deformation behaviors, which can better inform strategies for preserving this significant masonry structure.

The current research on the load-bearing and deformation characteristics of brick and stone masonry structures primarily focuses on structures with uniform cross-sectional properties. Najafgholipour et al. [1] studied the deformation of these structures under coupled in-plane and out-of-plane loads, while Addessi et al. [2] explored the response and damage characteristics under seismic loads, using both a shaking table and nonlinear finite element simulations. Pereira et al. [3] and Wang [4] analyzed the in-plane loading deformation characteristics and the influence of mortar joint technology on the retrofit of the ancient seawall, respectively, through experiments and numerical simulations. For unreinforced structures, Wilding [5] studied the impacts of load history on in-plane force-displacement response characteristics. Other researchers, like Taesung et al. [6], Abul Hasnat [7], and Gatta et al. [8], have utilized numerical simulations and theoretical analysis to understand the cyclic shaking, in-plane static deformation characteristics, and the nonlinear static and dynamic response of walls. Wilding et al. [9] proposed a theoretical formula for the shear modulus to elastic modulus ratio and explored its influence on the deformation of walls. While these studies have provided valuable insights, they have primarily concentrated on structures with uniform cross-sections. The Qiantang River ancient seawall, however, being a trapezoidal-sectioned stone masonry structure, has markedly different stress-deformation responses.

The cultural relics prohibits the direct mechanical testing on the original structure. Most existing research, therefore, relies on numerical simulations or experimental testing to study the stress and deformation characteristics of masonry structures of cultural relics. Due to the efficiency of modeling the complex geometry and nonlinear material behaviors that are intrinsic to masonry structure, the finite element method is commonly adopted. Ideally speaking, the masonry element (e.g., piers and spandrels) should be discretized by finite elements, respectively, for the brick/block units and mortar joints, which leads to the so-called micro-modeling approach [10,11]. When the mortar joint (of physical thickness) is modeled by a zero-thickness interface element, the so-called simplified micro-modeling approach is arrived [12]. Both the micro- and simplified micro-modeling approaches require refined finite element mesh, which causes a heavy computation burden. As an alternative, a macro-modeling approach was proposed in the literature [13,14], where a single element based on springs is used to model the entire masonry element. To overcome the common limitation of microelements in modeling the out-of-plane behavior of masonry structures, Vanin et al. [15] extended the 2D microelement to the 3D version, which was

successfully used in modeling unreinforced masonry buildings. The usefulness of a 3D microelement has been demonstrated in the literature, particularly for seismic loading conditions [16–19], which inevitably invoke the coupling of in-plane and out-of-plane behaviors of masonry structures. Through reduced-scale specimen tests, Osmanovic and Hrasnica [20] compared seismic responses and damage levels under different structural forms of wall. Kheyroddin et al. [21], Bocca et al. [22], Peng et al. [23], and Chen et al. [24] focused on strengthening measures, such as the use of fiber-reinforced polymers, desiccant repair mortars, ultra-high-performance concrete (UHPC), and oyster shell ash mortar. However, the distinct nature of ancient walls in terms of structure, building materials, and service environment warrants specific research, i.e., the research outcomes from other masonry structures may not be directly applicable to the Qiantang River ancient seawall.

The Qiantang River ancient seawall, facing the impact of tidal waves on its seaward side and soil pressure on its embankment side, shares similarities with the retaining walls. Most previous studies on retaining walls, such as stone walls [25,26], backfill soils [27], and reinforced earth retaining walls [28], have focused on horizontal loads, including soil pressure [29] and seismic forces [30]. Less attention has been given to vertical loads, such as vehicle-induced pressure on the wall's top [31]. In response to rising sea levels and increasingly frequent storm surges due to global warming, the ancient Qiantang River seawall is undergoing upgrade operations to increase its flood prevention standards. As construction machinery and materials will inevitably exert vertical loads on the wall during this process, urgent research into the vertical load-bearing and deformation traits of the seawall is needed.

In this regard, a 1:4 scale specimen of the ancient Qiantang River seawall was constructed for vertical monotonic, cyclic, and failure load testing. Servo actuators and laser displacement sensors were used to record loading force and displacement, while particle image velocimetry (PIV) captured the deformation field during loading. This analysis provided insights into vertical loading deformation development, vertical stiffness cyclic attenuation law, and wall vertical bearing failure characteristics of the ancient seawall. Such research results can provide guidance for the upgrading and protection of the Qiantang River ancient seawall.

2. Engineering Background

The Qiantang River ancient seawall measures 5.4 m in height and has a base width of 3.8 m. This wall comprises 17 layers of stones, arranged in a step-like fashion, with each layer progressively receding from the bottom towards the top. The topmost layer has a width of 1.44 m. The stones, each 0.32 m thick and 0.38 m wide, are assembled in an interlocking pattern. These stones are bound together using sticky rice lime mortar, as illustrated in Figure 2. The lengths of these stones range from 78 to 166 cm, thus creating a periodic pattern approximately 3.8 m in length parallel to the embankment (Figure 2). To adapt more effectively to the challenges presented by climate change, the Qiantang River ancient seawall is currently under retrofit and upgrading. During this construction process, the seawall may be subjected to vertical loads, such as embankment surcharge and vehicle loads, as depicted in Figure 3. Consequently, it is important to understand the vertical force–deformation characteristics of the ancient seawall.



Figure 2. Periodicity of construction structure of Qiantang River ancient seawall along the longitudinal direction.



Figure 3. Embankment load during the upgrading operations of Qiantang River ancient seawall.

3. Reduced-Scale Specimen Test

3.1. Reduced-Scale Specimen of the Ancient Seawall

A scaled-down specimen was created at a dimension ratio of 1:4, as shown in Figure 4. The specimen features a trapezoidal cross-section in the transverse direction, composed of 17 layers of stones that gradually reduce in width from the base to the crest (Figure 4a). The longitudinal representation of the specimen encapsulates one cycle of the prototype (Figure 4b). The base of the specimen spans 0.96 m, while the top measures 0.36 m. The specimen stands at a height of 1.36 m, with a longitudinal length of 0.95 m. The specimen was built using 371 stone blocks, each with cross-sectional dimensions of 950 mm × 800 mm. However, there were 20 unique stone lengths. The sizes and quantities of each stone type are detailed in Table 1, and the stone tags in Figure 4 correspond to the stone types in Table 1.

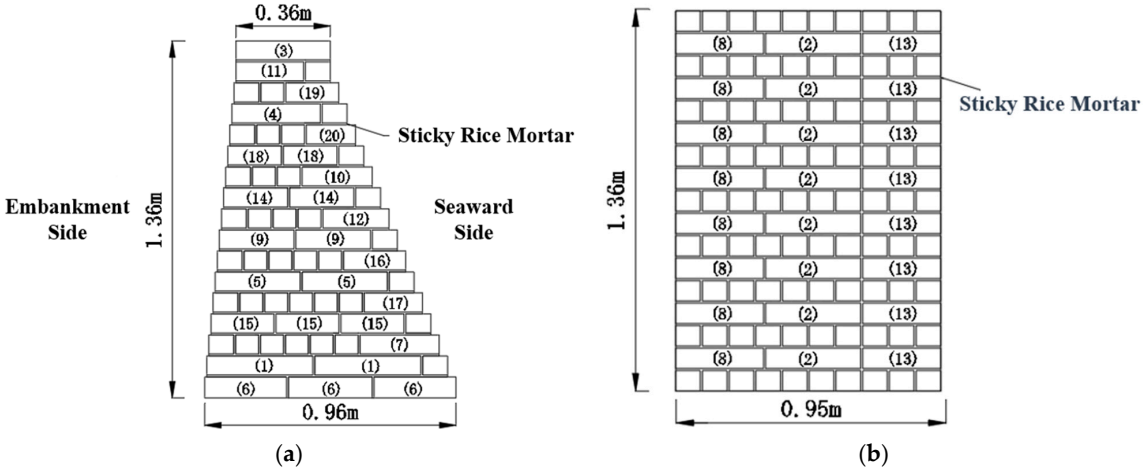


Figure 4. Dimensions of the reduced-scale specimen of ancient seawall: (**a**) lateral view; (**b**) front view.

Table 1. Dimensions of stone blocks for the reduced-scale specimen of ancient seawall.

Stone Type	Length (mm)	Quantity	Stone Type	Length (mm)	Quantity
(1)	413	20	(11)	265	10
(2)	390	37	(12)	260	10
(3)	360	10	(13)	255	37
(4)	345	10	(14)	253	20
(5)	333	20	(15)	249	30
(6)	320	30	(16)	245	10
(7)	310	10	(17)	230	10
(8)	305	37	(18)	213	20
(9)	293	20	(19)	210	10
(10)	275	10	(20)	195	10

3.2. Correspondence between Reduced-Scale Specimen and Full-Scale Seawall

The basic quantities chosen are the elastic modulus E, mass density ρ, and geometry dimension L, with respective dimensions of $[M][L]^{-1}[T]^{-2}$, $[M][L]^{-3}$, and [L]. To facilitate specimen construction, the materials for the specimen—both stone and mortar—replicate those of the original structure, only with the geometry dimension L scaled down by a factor of 1:4. The correspondence between the specimen and the full-scale structure is presented in Table 2.

Table 2. Correspondence between the reduced-scale specimen and full-scale structure of the Qiantang River ancient seawall.

Type	Physical Quantity	Dimension	Scale Ratio
Geometric Parameters	Length	L	1:4
	Displacement	L	1:4
	Area	L^2	1:16
Mechanical Parameters	Surface Load	$ML^{-1}T^{-2}$	1:1
	Stiffness	$ML^{-1}T^{-2}$	1:1

3.3. Stone Blocks

Figure 5 presents a core sample from the original stone blocks of the Qiantang River ancient seawall, confirming their lithology as granite. Because the seawall is a protected cultural relic, its original stone blocks could not be directly employed to construct the reduced-scale specimen for this study. Instead, we adopted weathered granite stones in constructing the specimen (as shown in Figure 6). Ultrasonic wave tests were conducted on the rock samples from both the real structure and the specimen (refer to Figure 7) to calculate their respective elastic modulus. These tests revealed that the elastic modulus of the real stone blocks was 517.5 GPa, while the stones of the specimen measured at 506.7 GPa. This 2% discrepancy suggests that the elastic properties of the stones of the reduced-scale specimen and the full-scale structure were essentially equivalent.



Figure 5. Photograph of core sample from Qiantang River ancient seawall.



Figure 6. Weathered granite blocks used in reduced-scale specimen construction.



Figure 7. Ultrasonic testing on rock samples.

3.4. Rice Mortar

The original Qiantang River ancient seawall employed rice mortar as an adhesive, which is made by mixing lime, rice paste, and water at a mass ratio of 20:1:14 [32]. Accordingly, the reduced-scale specimen in this study also utilized rice mortar as the adhesive, adhering to the same ratio as the prototype. The rice paste was prepared by combining rice flour and water and boiling the mixture for two hours. Subsequently, the lime, rice paste, and water were weighed according to the ratio and uniformly mixed to yield the required rice mortar (refer to Figure 8). The total volume of rice mortar used in the experiment amounted to approximately 23,000 cm^3.



Figure 8. Laboratory preparation of sticky rice mortar.

3.5. Curing of Specimen

Upon the completion of the specimen, it was subjected to a ten-day curing process while maintaining a constant temperature of 17 °C and humidity of 75%. During this curing period, the mortar experienced progressive strength growth. To monitor the curing process, dynamic tests were performed on the 3rd and 8th days. A hammer was employed to apply vertical impacts to the wall, while a velocity sensor captured the wall's vibration. The excitation and sensor points were positioned at the third layer on both sides of the wall (refer to Figure 9). The velocity sensor had a sampling frequency of 200 Hz, and a passband from 1 to 80 Hz.

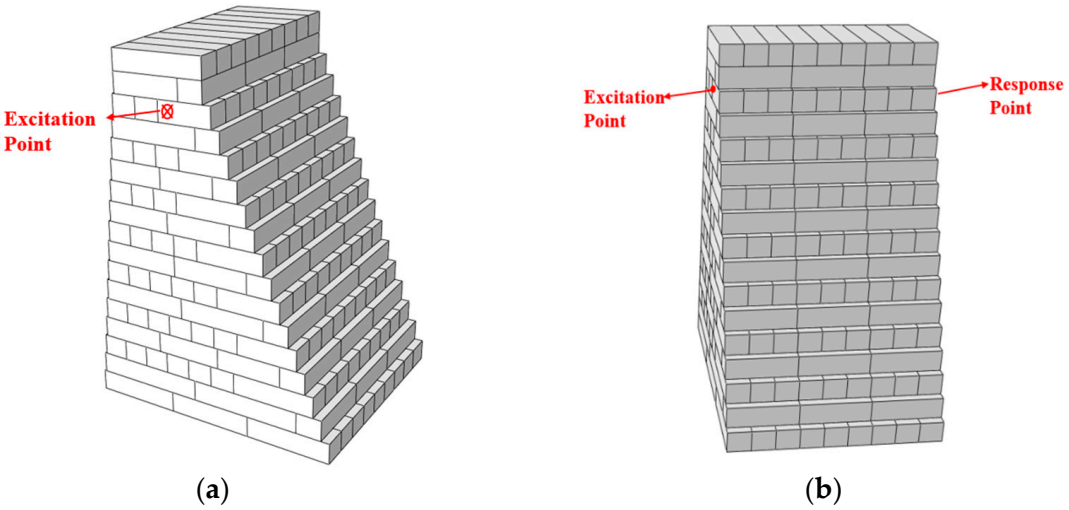


Figure 9. Schematic diagram of excitation point and response point locations in dynamic testing of the specimen (**a**) lateral view; (**b**) front view.

The vertical excitation force and vertical vibration velocity data were converted into the frequency domain. Dividing these two yielded the frequency response function of the ancient seawall (see Figure 10). Notably, the overlapping curves from the 3rd to 8th days of curing suggest that the mortar had completed its hardening process, indicating the full curing of the specimen.

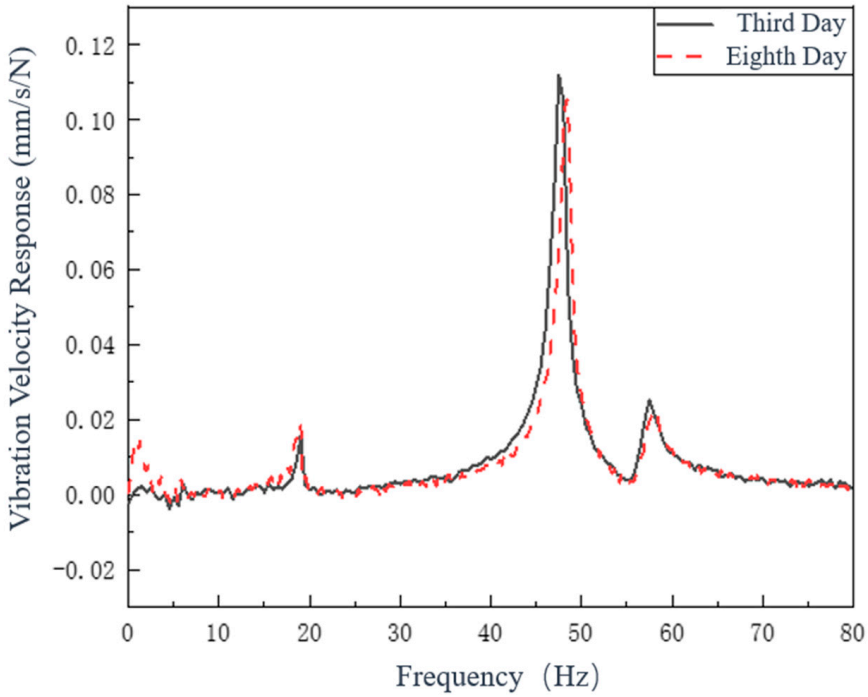


Figure 10. Frequency response function of the specimen.

3.6. Loading Device

A large-span loading system, independently developed by the Zhejiang University of Technology, was employed for vertical loading, as shown in Figure 11. This system comprises two electro-hydraulic servo actuators linked to rigid loading beams; the downward displacement of the actuator pushes the beams, which provides a compressive load to the specimen. The system automatically logs the loading force and displacement, with a maximum force of 2000 kN and a displacement of 250 mm. The accuracy of the force

measurement is ±1% of the displayed value, while the displacement measurement accuracy is 0.1% FS. To mitigate the rate effect of loading, the experiment was conducted at a slow loading rate of 0.5 mm/min.



(**a**) (**b**)

Figure 11. Reduced-scale specimen test setup: (**a**) lateral view; (**b**) overall view.

A load distribution beam, fabricated from I-section steel with cross-section dimensions of 250 mm × 350 mm, was positioned between the wall's top and the loading beam, ensuring uniformly distributed loads. When the center of the load distribution beam was aligned with the center of gravity of the ancient seawall structure, it ensured axial compression. To augment the stiffness of the load distribution beam, web plates were periodically welded at 0.2 m intervals along the length. Given the unevenness of the top surface of the wall due to construction errors, a thin layer of sand was spread between the bottom of the distribution beam and the seawall's top for leveling purposes.

3.7. Monitoring Devices

A laser displacement sensor was used to measure the vertical displacement at the top of the seawall. As depicted in Figure 11b, the sensor was located directly under the distribution beam. The laser sensor has a measuring range of 210 mm, an accuracy of 75 μm, and an 8 Hz sampling frequency.

To track the deformation field of the front and side surfaces of the seawall, particle image velocimetry (PIV) was utilized. PIV, a two-dimensional displacement measurement technique based on image cross-correlation analysis, captures images at a high frequency and extracts the deformation field via pixel-wise cross-correlation algorithms.

Figure 12 illustrates the placement of PIV cameras on the front and left sides of the wall. Control points were marked on the wall surface for subsequent image processing. With a 5 Hz frequency, the front camera's field of view covered an area of 38 cm × 80 cm, encompassing half the front surface of the wall, with an image resolution of 4912 × 3684 pixels. The side camera's field of view, covering an area of 100 cm × 100 cm, fully encompassed the wall's side surface, yielding an image resolution of 5496 × 3672 pixels.

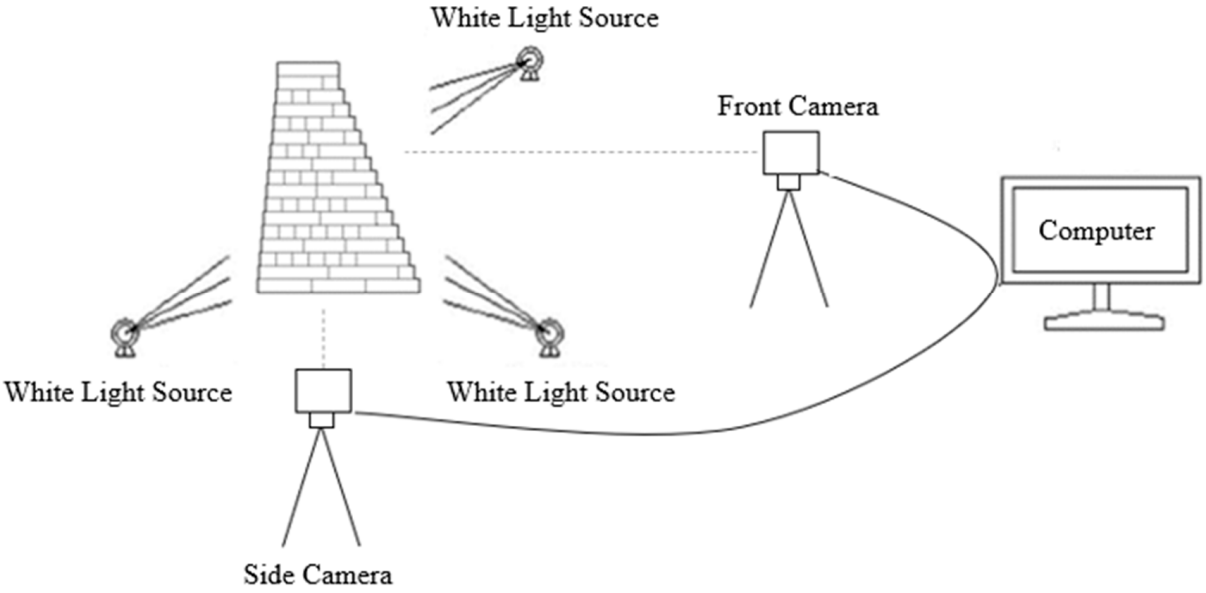


Figure 12. Schematic of particle image velocimetry (PIV) system.

3.8. Loading Scheme

To guide the loading parameters, we built a finite element model of the reduced-scale specimen in ABAQUS. A displacement-controlled loading was applied to the top of the numerical seawall. From the numerical modeling, the ultimate bearing capacity of the seawall specimen was found as F_u = 1700 kN, which corresponds to a uniformly distributed load of 4.4 MPa on the wall's top. More details of the numerical simulation are given in Appendix A.

Based on F_u, a loading scheme for the seawall specimen was established. This scheme entailed preloading the wall to eliminate gaps between the loading apparatus and the specimen, thereby ensuring complete contact between the loading beam, distribution beam, and the wall's top. When the loading device first touched the wall, the actuator load, F_c, was approximately zero, with the corresponding displacement denoted as δ_c. This was followed by monotonic loading, with the maximum load, F_m, set to 30% of the ultimate load ($F_m = 0.3F_u$ = 450 kN), and the associated actuator displacement represented as δ_m. Afterwards, displacement-controlled cyclic loading was performed for 10 cycles between δ_c and δ_m, resulting in cyclical variations in the actuator load, F_c. The final stage involved monotonic loading until either the specimen failed or the load limit of the loading system was reached. The maximum load and displacement in the final stage are denoted as F_f and δ_f, respectively.

The successive stages of loading are depicted in Figure 13. Given that the maximum load during the monotonic loading stage (F_m) was maintained at only 30% of the ultimate bearing capacity (F_u), it is reasonable to assume that the specimen remained within the linear elastic stage (this is also confirmed by the numerical modeling in Appendix A), and thus, did not influence the subsequent cyclic loading.

Cyclic loading in the test was included mainly for modeling the cyclic construction loads (e.g., traffic loads) on the top of the seawall. However, over a long-term window (i.e., exceeding 30 years), it has been observed that transportation conditions and hydrological phenomena induced by urbanization and other factors (e.g., Feng et al. [33]) exhibit inherent variability, such as tidal depths and river velocities (e.g., Dimitriadis et al. [34]), through clustering mechanisms (specifically, the Hurst phenomenon and HK dynamics). So, hydrological phenomena (e.g., tidal depths and river velocities) may play an equal role as the construction loads in causing the stability and safety problems of the ancient seawall. The clustering effect of the construction load and the hydrological load on the seawall can be simulated as continuous cycles of varying magnitudes. Thus, the cyclic

loading in the test can also have implications in revealing the clustering mechanisms of the ancient seawall. Since the maximum load in the cyclic loading stage is F_m (=0.3 F_u), the normal service state for the Qiantang River ancient seawall under repetitive loads can be represented in the laboratory. Based on the cyclic loading, the small-strain cyclic stiffness of the specimen can be determined. Under the requirements of cultural heritage preservation, the seawall should retain a small-strain state during tidal surges or construction cyclic loads, without structural failure.

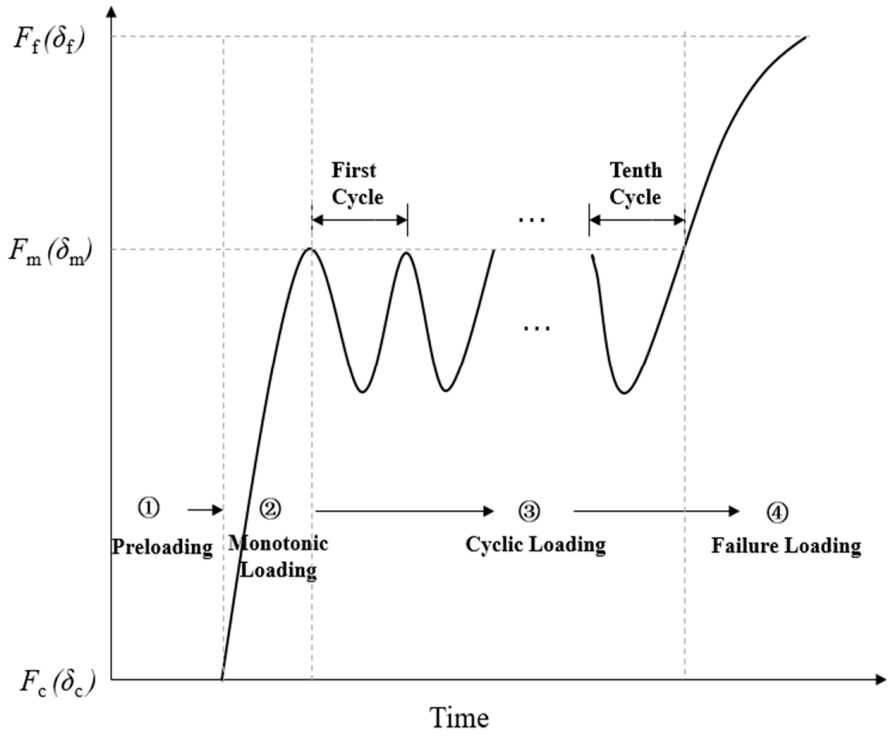


Figure 13. Schematic of vertical loading process for the seawall specimen.

The final failure loading stage provided crucial data on the ultimate bearing capacity and deformation failure development pattern of the seawall, thereby serving as a benchmark for determining the maximum surcharge pressure on the wall's top in practical engineering applications.

4. Experimental Results and Analysis

4.1. Overall Situation

The loading process for the seawall specimen, corresponding to the previously described loading scheme, is depicted in Figure 14. The distinct stages of preloading, monotonic loading, cyclic loading, failure loading, and subsequent unloading are clearly marked in the figure. It can be noted that during the preloading stage, the actuator output, F_c, was approximately zero. The monotonic loading stage saw the actuator output increase linearly until it reached a peak at $F_m \approx 450$ kN. The cyclic loading stage saw a reduction in the peak actuator output, F_c, from 450 kN in the first cycle to 345 kN in the tenth cycle. During the failure loading stage, the maximum actuator output reached 1800 kN, nearly matching the maximum effective load capacity of the actuator (i.e., 2000 kN). Nonetheless, the specimen did not display severe overall failure, such as extensive fracturing or collapse, but only revealed localized damage, including mortar joint cracks and block stone fractures. Unloading was initiated to protect the loading apparatus once the vertical load on the actuator reached 1800 kN.

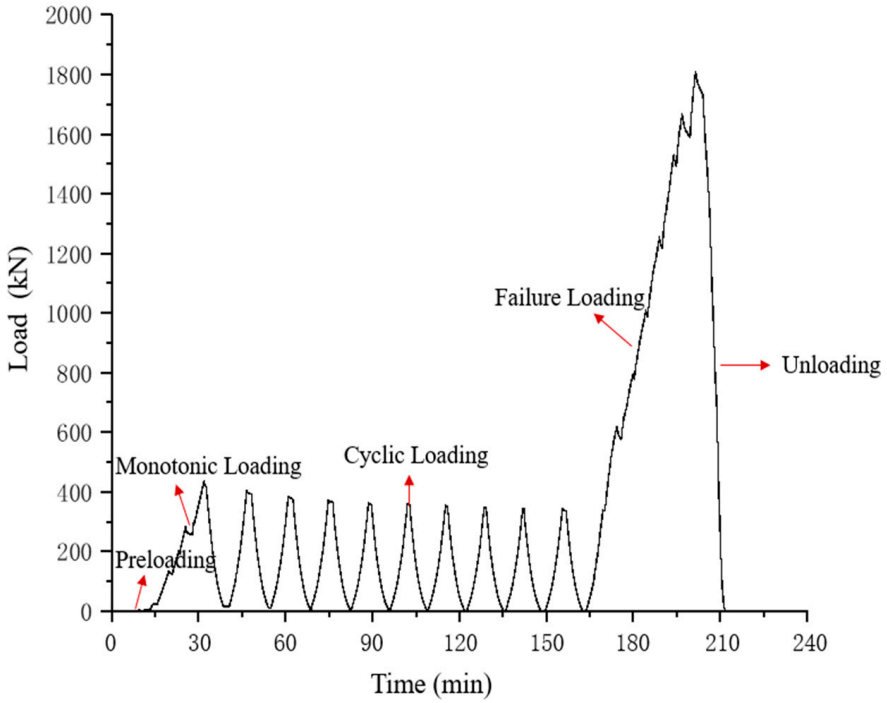


Figure 14. Time–history curve of vertical load on the top of the seawall specimen.

The vertical displacement–time history curves of the actuator and the top of the specimen are presented in Figures 15 and 16, respectively. The loading beam and distribution beam, which are located between the actuator and the wall's top, would also deform under the vertical load. Consequently, the maximum displacement of the actuator during the experiment was 20 mm, while the corresponding maximum vertical displacement of the wall's top was merely 11.6 mm, resulting in a discrepancy of 8.4 mm.

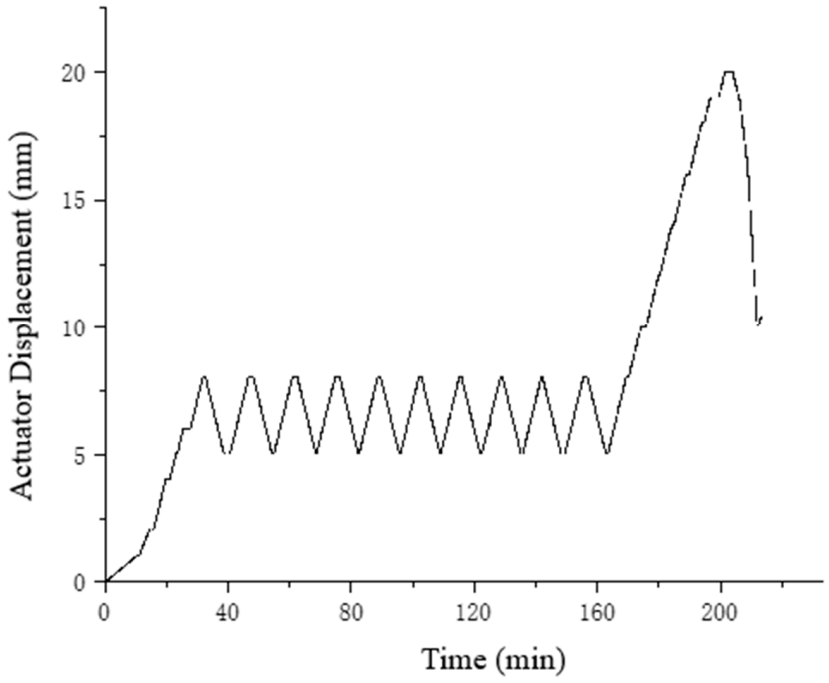


Figure 15. Time–history curve of actuator displacement.

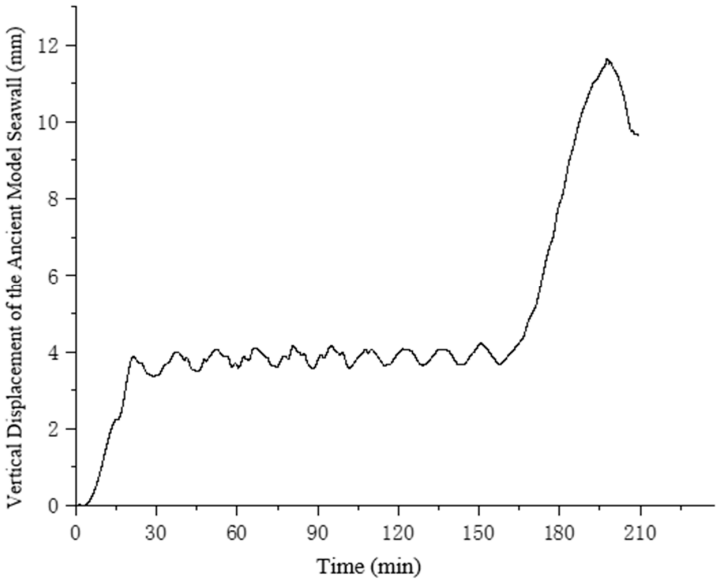


Figure 16. Time-history curve of vertical displacement on the top of the seawall specimen.

The deformation of the ancient seawall during the vertical loading process can be distinctly classified into three stages. The monotonic loading stage manifested no notable alteration in the wall's appearance, except for sporadic peeling of the surface layer of mortar joints. During the cyclic loading stage, certain surface layers of mortar joints exhibited peeling, along with the detachment of some mortar powder and the appearance of cracks within the vertical mortar joints. In the initial phase of the failure loading stage (i.e., the actuator displacement from +8 mm to +16 mm), minor vertical cracks began to appear in some stones, while there was significant detachment of the mortar powder. In the subsequent phase of the failure loading stage (i.e., the actuator displacement from +16 mm to +20 mm), the cracks in the stones rapidly expanded, and more stones started displaying vertical fracture cracks. Meanwhile, the cracks in the mortar joints broadened, and compression noises emanated from within the wall. Figures 17–19 feature representative photographs of the wall at each stage.



Figure 17. Photograph of the ancient seawall during monotonic loading stage (no observable failure either in mortar joints or stones).



Figure 18. Photograph of the ancient seawall during cyclic loading stage.

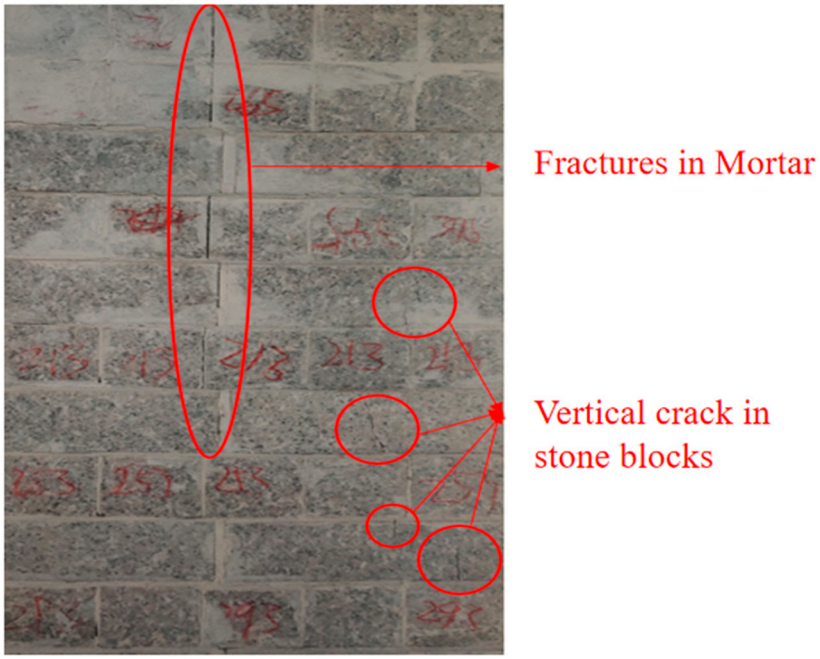


Figure 19. Photograph of the ancient seawall during failure loading stage.

The force–displacement curve of the wall top throughout the loading process is depicted in Figure 20. It was observed that the peak loads during the monotonic and cyclic loading stages approximately constituted 23% of the maximum load in the failure loading stage. Additionally, throughout the failure loading stage, the load increased proportionately with the displacement of the wall top, and the curve does not display a clear yield point. The wall structure manifested several surface cracks, suggesting that the specimen did not undergo an overall structural failure. When the load reached its maximum of 1800 kN, the greatest vertical displacement of the wall top was 11.63 mm, with a residual displacement of 5 mm after unloading.

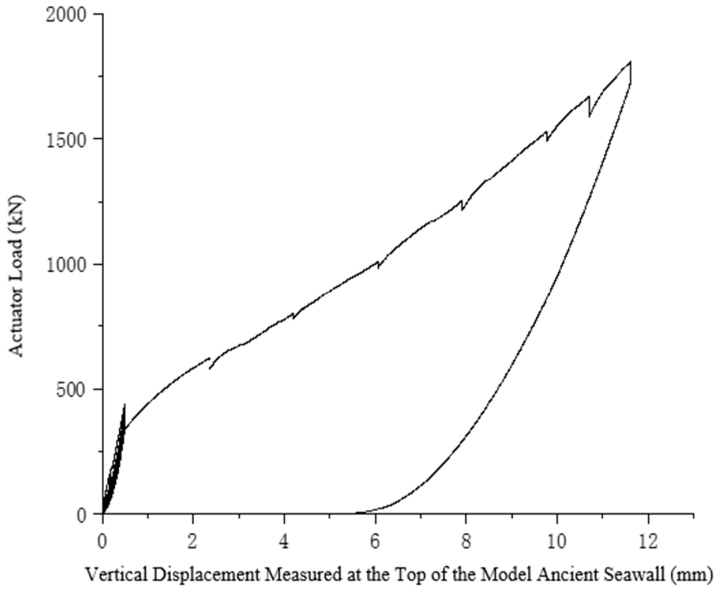


Figure 20. Load–displacement curve of the top of the seawall specimen.

4.2. Deformation Field Analysis of the Ancient Seawall

By conducting a cross-correlation analysis between the images of the wall taken prior to the experiment and those taken at the end of the failure loading stage, the displacement field of the ancient seawall throughout at the final step of the test was obtained, as illustrated in Figure 21. The figure reveals that deformation of the ancient seawall was primarily localized in the upper half, notably within a length of 0.5 times the width of the wall top, which absorbed 85% of the wall top displacement. Beyond the vertical downward displacement, the seawall also presented a horizontal displacement directed towards the embankment side, as demonstrated in Figure 22. Given the trapezoidal cross-sectional shape of the seawall and the displacement constraint imposed by the distribution beams on the wall top, the horizontal displacement of the wall peaks at 4.4 mm on the embankment side at a distance of 0.21 m from the wall top. This observation indicates that under the vertical loading on the wall top, the wall exhibited an inclination to overturn towards the embankment side, which is in accordance with the numerical simulation results presented in Figure A7 of Appendix A.

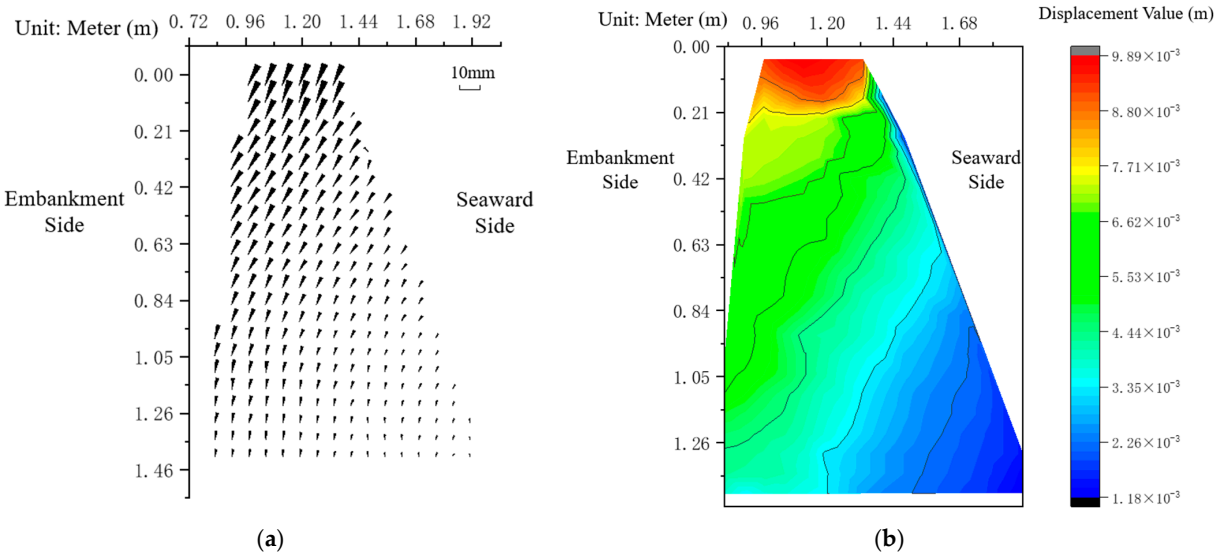


Figure 21. Side view of displacement field of the final step of the test on the ancient seawall: (**a**) vector map; (**b**) vertical displacement contour map.

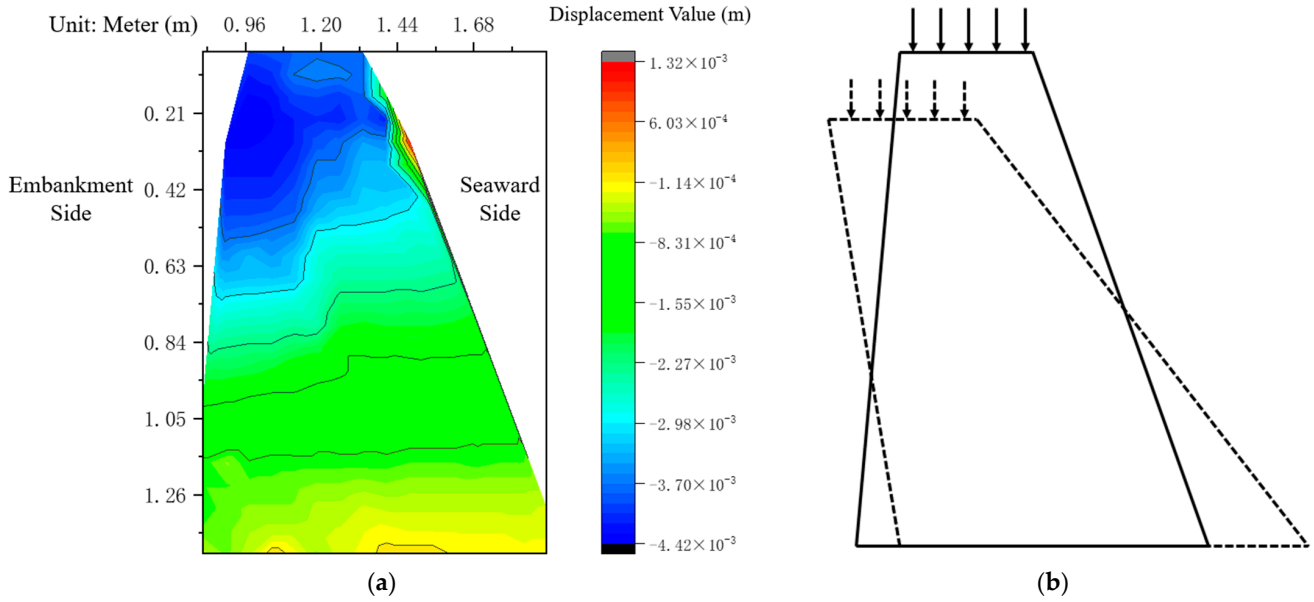


Figure 22. Side view of displacement field at the final step of the test on the ancient seawall: (**a**) horizontal displacement contour map; (**b**) schematic of deformation pattern.

Figures 23 and 24 present the vertical displacement fields of the ancient seawall during the monotonic loading and failure loading stages, respectively. It was observed that the wall top displacements during these stages were 3 mm and 7 mm, respectively, which is consistent with the measurements obtained from the laser displacement sensors (refer to Figure 16). Figure 23a indicates that during the monotonic loading stage, deformation of the wall was largely contained within a length of 0.5 times the width of the wall top.

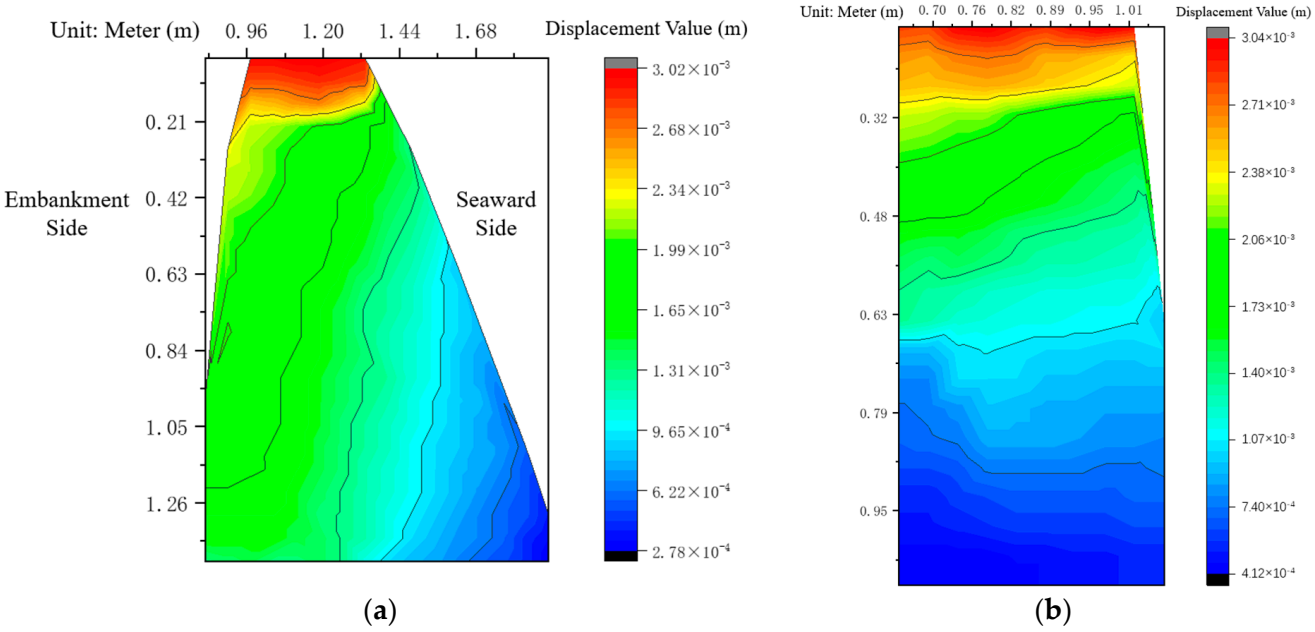


Figure 23. Vertical displacement contour map of the specimen during monotonic loading process: (**a**) side view; (**b**) front view.

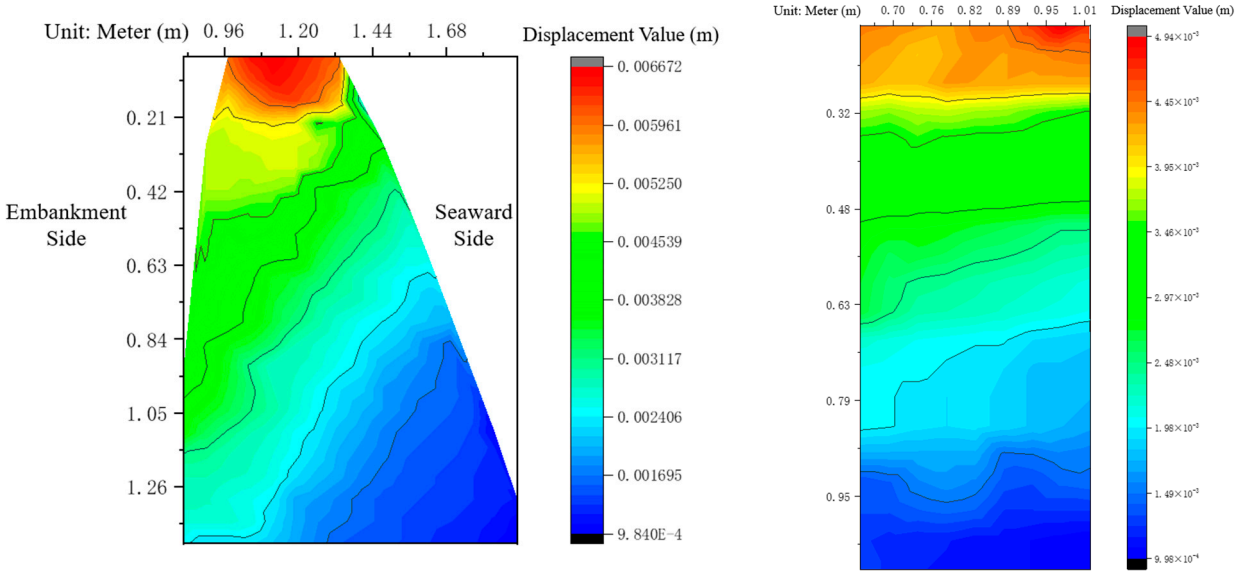


Figure 24. Vertical displacement contour map of the specimen at the final step of the test: (**a**) side view; (**b**) front view.

Figures 25 and 26 show the horizontal displacement fields of the ancient seawall during the monotonic loading and failure loading stages, respectively. The positive and negative values indicate displacements towards the seaward and embankment sides, respectively. Comparative analysis indicates that the horizontal deformation range of the wall during the failure loading stage expanded from 0.5 times the width of the wall top to 1.5 times, suggesting a more marked lateral overturning tendency.

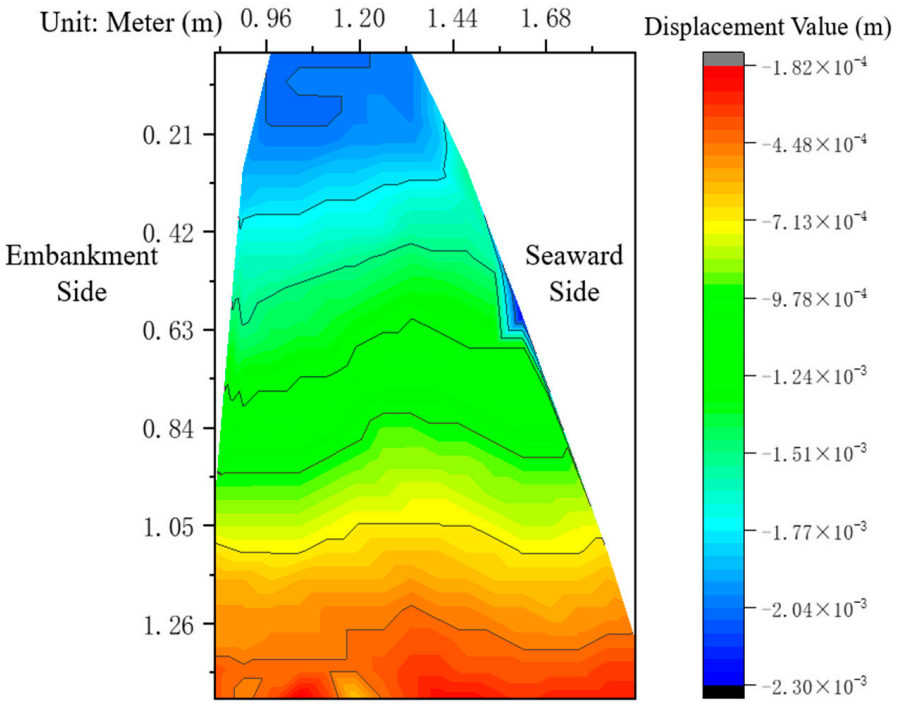


Figure 25. Horizontal displacement contour map of the specimen during monotonic loading process.

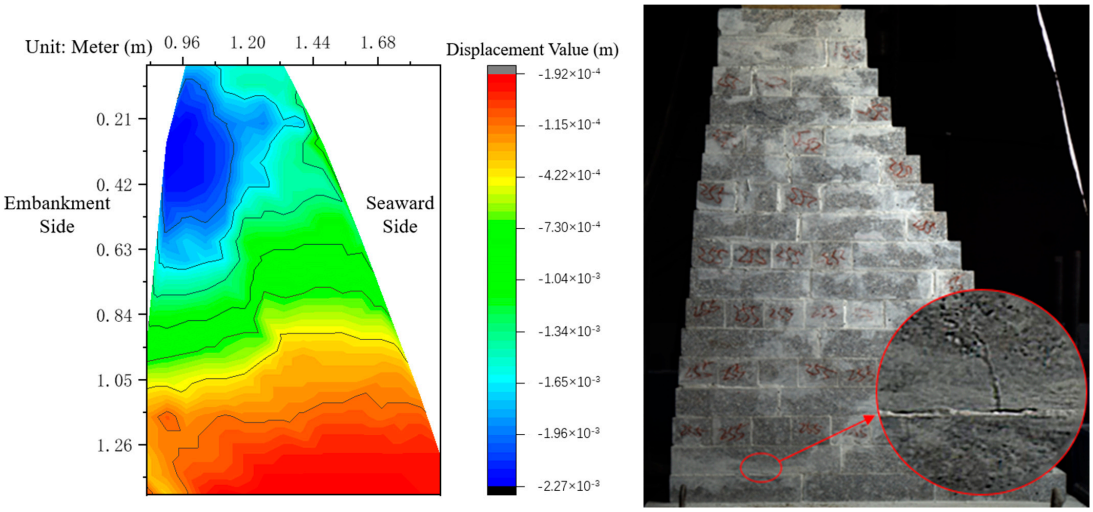


Figure 26. Side view of horizontal displacement contour map and photograph during failure loading stage of the specimen: (**a**) contour map; (**b**) photograph.

Regions with opposite signs of horizontal displacements in Figures 25 and 26 denote locations where cracks emerged. PIV image analysis revealed that no cracks materialized in the stones and mortar during the monotonic loading stage. However, during the failure loading stage, vertical cracks appeared in the stone (Stone Type (1), see Figure 4) near the bottom of the ancient seawall when the load approximated 560 kN. As the load increased, the cracks persistently expanded and deepened. Figure 26 presents a comparison between the horizontal displacement contour and the crack images. When the vertical load during the failure loading stage escalated to 685 kN, distinct vertical cracks appeared in the mortar layers and stone in the middle of the ancient seawall. Figure 27 exhibits a comparison between the horizontal displacement contour and the crack images observed from the front of the specimen.

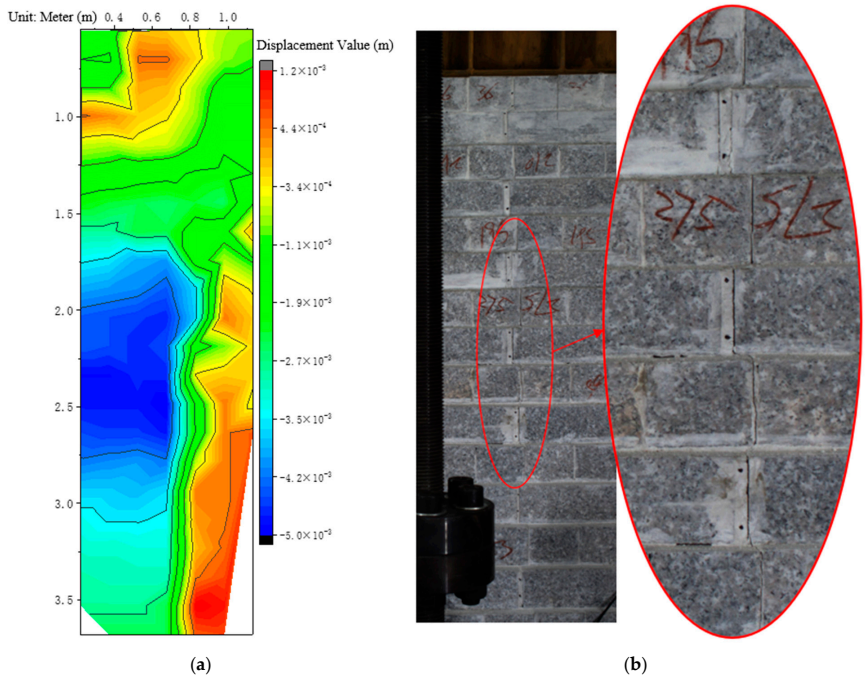


Figure 27. Front view of horizontal displacement contour map and photograph during failure loading stage of the specimen: (**a**) contour map; (**b**) photograph.

In comparison to the monotonic loading stage, the peak values of horizontal and vertical displacements during the failure loading stage escalated by 98% and 221%, respectively, signifying that the vertical displacement of the wall was more responsive to the increments of vertical load on the top of the ancient seawall.

4.3. Stiffness Degradation of the Ancient Seawall

Figure 28 presents the load–displacement curve during the cyclic loading stage, which exhibits distinct hysteresis loops. The slope of the line linking the top and bottom points of each hysteresis loop represents the vertical stiffness of the specimen, while the area contained within the hysteresis loop illustrates the damping. As demonstrated in Figure 29, the vertical stiffness of the ancient seawall exhibited continuous variation with the number of cycles, i.e., the vertical stiffness of the ancient seawall decreased from 760 kN/mm^2 to 684 kN/mm^2. The vertical load during the cyclic loading stage, F_c, was relatively small, significantly lower than the failure strength of the seawall. Therefore, the stiffness degradation of the ancient seawall was predominantly attributed to the cyclic weakening of the mortar layers. This softening of the mortar stiffness resulted in cumulative displacement of the mortar joints, leaving a residual displacement of 0.3 mm at the wall top at the end of the cyclic loading stage.

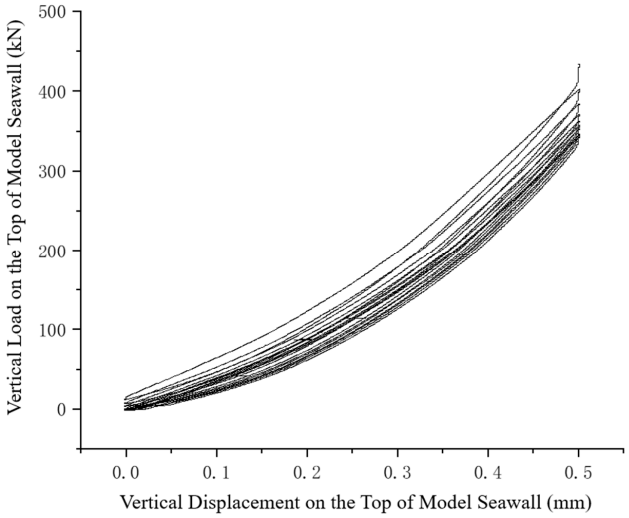


Figure 28. Load–displacement plot during the cyclic loading stage.

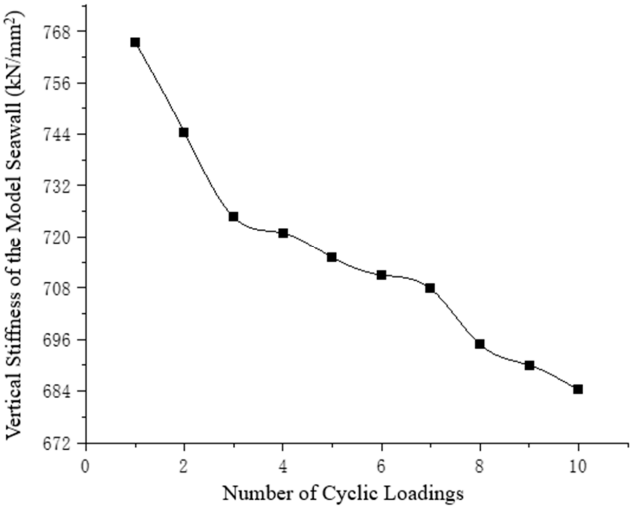


Figure 29. Variation of wall stiffness during the cyclic loading stage.

5. Discussion

Based on the experimental findings, neither the mortar nor the stones of the ancient seawall cracked when subjected to vertical loads up to 1.4 MPa (corresponding to F_m = 450 kN). However, the application of cyclic loads to the seawall, even when load amplitudes were maintained below 1.4 MPa, led to some visible cracking in the mortar layer. Under the maximum test load of 5.3 MPa (corresponding to F_f = 1800 kN), both the mortar and the stones of the ancient seawall displayed considerable cracking, and continuous vertical cracks even emerged. Despite this, the overall stability of the ancient seawall was preserved, and no structural failure (e.g., collapse) was observed. The Qiantang River ancient seawall is a nationally protected cultural relic, subject to heritage preservation laws that prohibit any cracking in both the mortar and the stones, not to mention overall structural failure. To adhere to heritage preservation requirements, the vertical load applied to the top of the Qiantang River ancient seawall should not exceed 1.4 MPa. If the load at the wall top exhibits cyclic characteristics (e.g., traffic loads), the limit for vertical loads should be reduced below 1.4 MPa to prevent cracking of the mortar.

The novelty of this study is obvious since the limit of vertical loading on top of the seawall is proposed for the first time. Given the elastic limit of 1.4 MPa and the typical contact area of the tire of 0.3 m^2, the axle load limit of a vehicle on the seawall can be as high as 34 t. For the retrofit project for the ancient seawall, the construction vehicle of the maximum total load is 70 t (note that the total load is distributed over five axles), which is significantly lower than the elastic limit of the seawall. Thus, we can reasonably infer that within the practically possible range of top loads (generally within 30 kPa), the Qiantang River ancient seawall will not experience an overall collapse or visible fractures in stone and mortar.

It is noted that the above suggestions are based on the experimental test involving only vertical loading to the wall. However, the real structure is also subjected to lateral soil pressure, as there is soil refilling at the embankment side of the wall. The deformation and stability characteristics and the associated load limits of the ancient seawall subjected to combined vertical (e.g., traffic load) and horizontal (i.e., soil pressure and water force (from tides and river velocities)) loadings will be the focus of future study.

6. Conclusions

This study introduced the distinctive material composition and structural design of the Qiantang River ancient seawall. A scaled-down specimen, at a scale-ratio of 1:4, was built to study the vertical monotonic loading, cyclic loading, and failure loading behaviors. The displacement field of the ancient seawall during the loading stages was obtained using particle image velocimetry (PIV) technology. The principal findings of this research are as follows:

(1) Throughout the monotonic loading stage (peak load value of 1.4 MPa), the specimen stayed in the linear elastic stage, with no observable cracking in the wall's mortar or stones.
(2) During the cyclic loading stage, the elastic behavior of the mortar deteriorated, leading to a reduction in the vertical stiffness of the specimen when the number of loading cycle increased. The vertical stiffness of the specimen reduced by 10% after ten loading cycles.
(3) Over the course of loading with a vertical load of 5.3 MPa at the top of the seawall, the wall underwent a maximum vertical displacement of 12 mm and a horizontal displacement of 5 mm. Vertical displacement was primarily observed in the upper half of the wall, within a range of 0.5 times the width of the wall top, whereas the horizontal displacement was concentrated in the upper half of the wall, within a range of 1.5 times the width of the wall top.
(4) As the vertical load at the top of the wall increased, the range of horizontal deformation dramatically extended, resulting in a tendency for the horizontal overturning of the seawall towards the embankment side.
(5) The predominant failure throughout the loading process was the cracking of the mortar. As the vertical load on the wall top increased in the range of 2.4–5.3 MPa,

vertical cracks emerged in stones near the bottom of the wall, and substantial vertical cracks appeared in the central section of the wall. Despite this, the ancient seawall did not undergo an overall structural failure (e.g., sudden collapse).

Author Contributions: Conceptualization, Q.C. and L.S.; methodology, Q.C., X.T., Y.L. and W.L.; formal analysis, Q.C., L.S., Y.L., X.T. and W.L.; investigation, W.L.; writing—original draft preparation, Q.C.; writing—review and editing, L.S.; visualization, X.T. and Y.L.; supervision, X.T. and Y.L. All authors have read and agreed to the published version of the manuscript.

Funding: This research received no external funding.

Data Availability Statement: The data presented in this study are available on request from the corresponding author.

Conflicts of Interest: The authors declare no conflict of interest.

Appendix A

Appendix A.1. Numerical Model and Parameters

Using the commercial finite element software ABAQUS (2022 Edition), we built a finite element model of the reduced-scale specimen, as shown in Figure A1. The stones were discretized using solid elements, and the mortar was modeled by the cohesive elements. The Drucker–Prager (DP) model was adopted to govern the mechanical behaviors of the stone. As for the mortar layer, its elastic response was based on a linear traction separation relationship, whereas its plastic response was governed by a quadratic stress criterion on the crack initiation and an energy-dissipation-based law on the crack propagation. The model parameters of the stones included a density of 2550 kg/m^3, a Young's modulus of 40 GPa, a Poisson's ratio of 0.2, a friction angle of 36°, a dilatancy angle of 11.3°, and a flow stress ratio of 1.0. As for the evolution of the yield stress with the absolute plastic strain (see Table A1), it was obtained through a laboratory triaxial test on the stone samples. The normal, shear, and tangential elastic moduli of the cohesive element representing the mortar are 5 GPa, 2 GPa, and 2 GPa, respectively. The tensile and shear strength of the mortar were set equal to 25 kPa and 35 kPa, respectively. The energies required for the evolution of normal and shear fractures were set equal to 18 J/m^2 and 125 J/m^2, respectively. The mass density of mortar was taken as 1800 kg/m^3.

The fixed boundary condition was applied to the bottom of the model. The central point (RP-1) on the top surface of the model was selected as the loading point. A rigid connection was specified between RP-1 and entire top surface of the model. The vertical load was applied in a displacement control manner. The target vertical displacement at the loading point RP-1 was −0.012 m, which corresponds to the peak displacement during the failure loading stage in the reduced-scale specimen test.

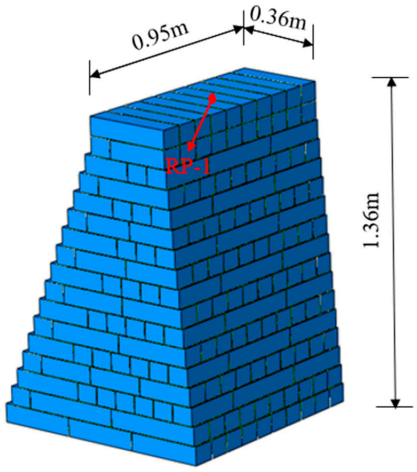


Figure A1. Schematic diagram of the numerical model of the reduced-scale specimen.

Table A1. Relationship between yield stress and plastic strain variation.

Yield Stress (MPa)	Absolute Plastic Strain
62.28	0
78.78	0.0005
95.99	0.001
113.07	0.0015
130.3	0.002
145.87	0.0025

Appendix A.2. Comparison and Analysis of Loading Results

From the numerical model, the variation of the vertical load with the loading displacement at RP-1 can be obtained. The maximum vertical load from the numerical modeling was equal to 1700 kN, which is quite close to the largest load (i.e., 1800 kN) obtained during the experimental test, as shown in Figure A2.

For the cohesive mortar layer, the node in the seventh layer from the top was selected as the observation point, as depicted in Figure A3. The degradation curve of mortar stiffness, as seen in Figure A4, was extracted. When the vertical displacement reached 4.2 mm, the stiffness of the top mortar layer degraded to zero, suggesting a failure of the mortar layer, which is consistent with the mortar cracks observed during the reduced-scale specimen tests.

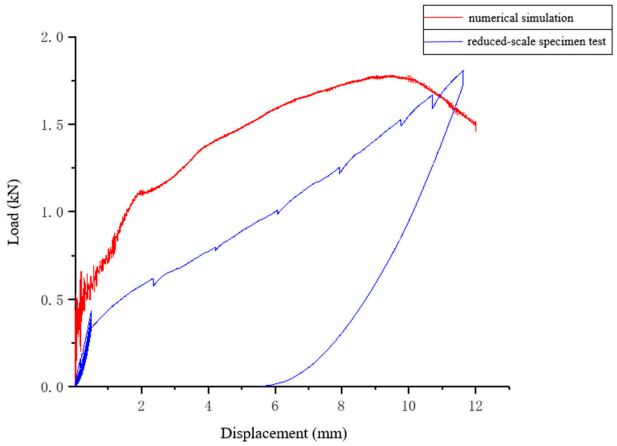


Figure A2. Force–displacement curve.

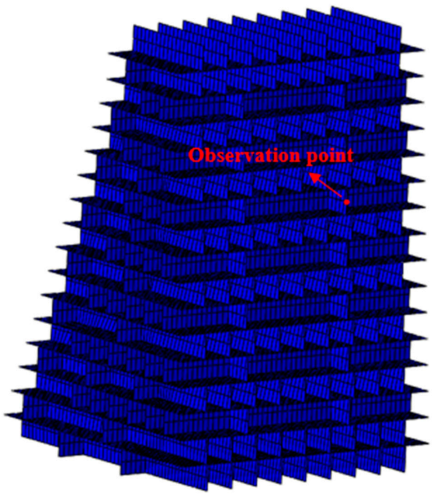


Figure A3. Selected observation point for stiffness degradation of the mortar layer.

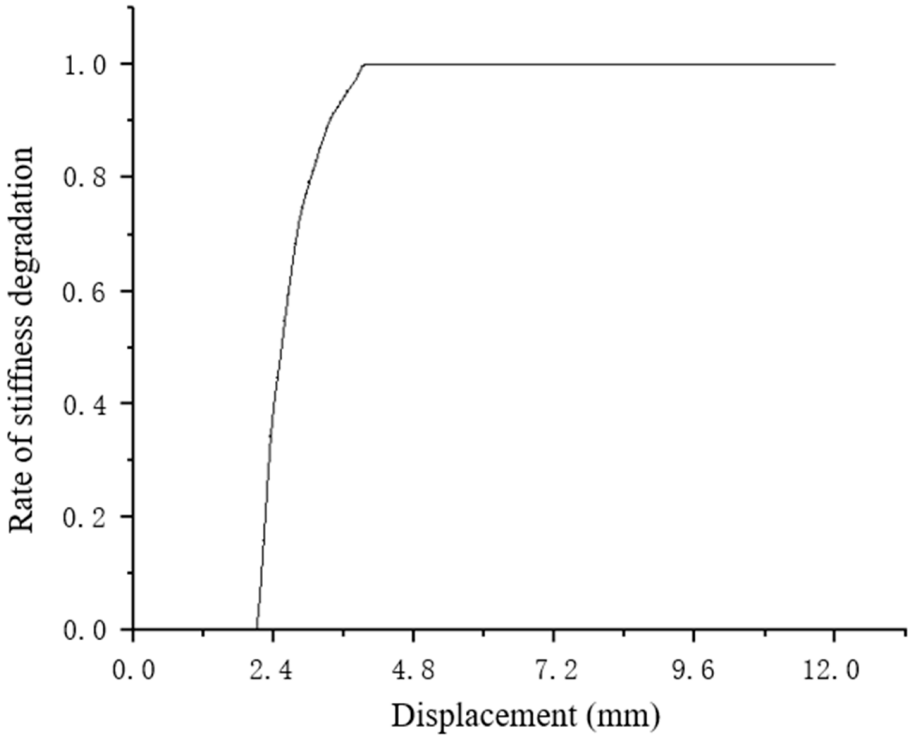


Figure A4. Stiffness degradation curve of the top mortar layer.

Figures A5 and A6 present the contour plots of horizontal and vertical displacements of the numerical model when the top vertical displacement was 0.012 m. The distribution pattern of the horizontal displacement field aligns with the experimental test, although the maximum vertical displacement value of 9 mm is slightly smaller than that of the reduced-scale specimen test (11.6 mm).

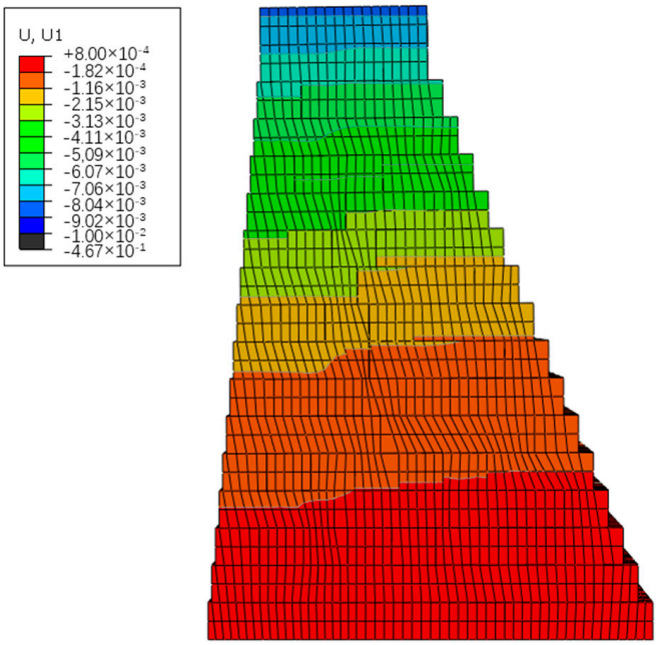


Figure A5. Horizontal displacement contour map of the numerical model under ultimate load.

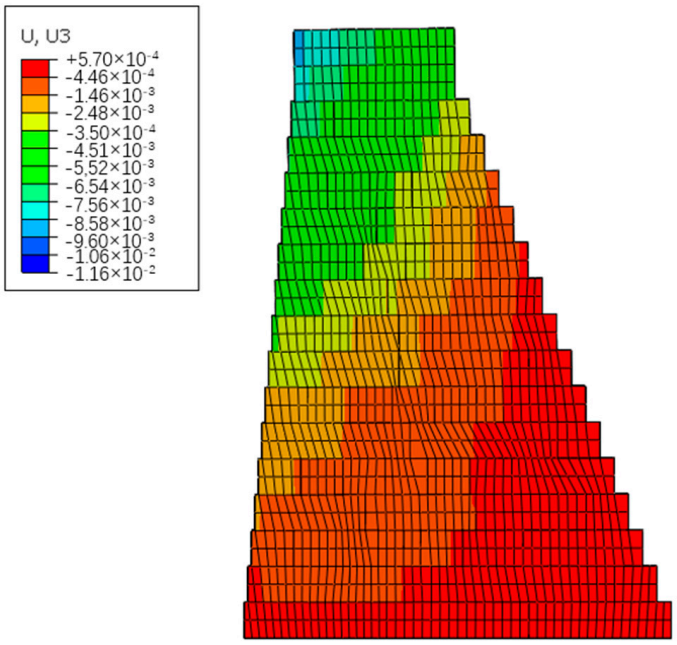


Figure A6. Vertical displacement contour map of the numerical model under ultimate load.

To validate the accuracy of the overturning mode derived from the reduced-scale specimen test, a comparison was conducted with the overturning mode of the numerical model, as depicted in Figure A7.

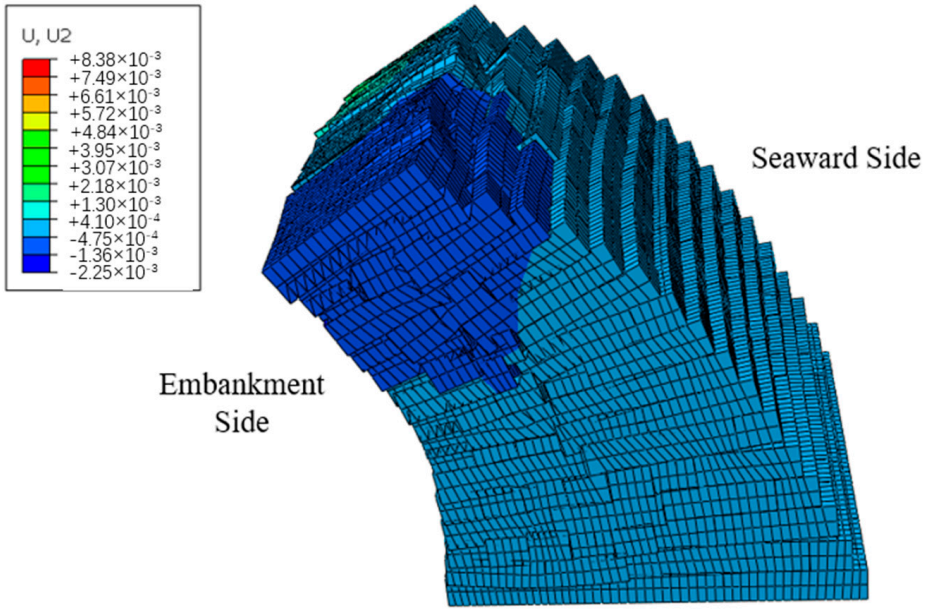


Figure A7. Overturning mode of the numerical model.

References

1. Najafgholipour, M.A.; Maheri, M.R.; Lourenco, P.B. Capacity interaction in brick masonry under simultaneous in-plane and out-of-plane loads. *Constr. Build. Mater.* **2013**, *38*, 619–626. [CrossRef]
2. Addessi, D.; Gatta, C.; Vestroni, F. Dynamic response of a damaging masonry wall. In Proceedings of the 10th International Conference on Structural Dynamics (EURODYN), Rome, Italy, 10–13 September 2017.
3. Pereira, J.M.; Correia, A.A.; Lourenco, P.B. In-plane behaviour of rubble stone masonry walls: Experimental, numerical and analytical approach. *Constr. Build. Mater.* **2021**, *271*, 121548. [CrossRef]

4. Wang, C.; Fort, J.P.; Nikitas, N.; Sarhosis, V. Retrofitting of masonry walls by using a mortar joint technique; experiments and numerical validation. *Eng. Struct.* **2016**, *117*, 58–70. [CrossRef]
5. Wilding, B.V.; Dolatshahi, K.M.; Beyer, K. Influence of load history on the force-displacement response of in-plane loaded unreinforced masonry walls. *Eng. Struct.* **2017**, *152*, 671–682. [CrossRef]
6. Taesung, E. Rocking Behavior of Unreinforced Masonry Walls Under Cyclic Load. *J. Earthq. Eng. Soc. Korea* **2023**, *27*, 49–57.
7. Hasnat, A. *Quasi Static In-Plane Behavior of Full Scale Unreinforced Masonry Wall with and without Retrofitting*; Bangladesh University of Engineering and Technology: Dhaka, Bangladesh, 2020.
8. Gatta, C.; Addessi, D.; Vestroni, F. Static and dynamic nonlinear response of masonry walls. *Int. J. Solids Struct.* **2018**, *155*, 291–303. [CrossRef]
9. Wilding, B.V.; Godio, M.; Beyer, K. The ratio of shear to elastic modulus of in-plane loaded masonry. *Mater. Struct.* **2020**, *53*, 40. [CrossRef] [PubMed]
10. Senthivel, R.; Lourenco, P.B. Finite element modeling of deformation characteristics of historical stone masonry shear walls. *Eng. Struct.* **2009**, *31*, 1930–1943. [CrossRef]
11. Furtmuller, T.; Adam, C. Numerical modeling of the in-plane behavior of historical brick masonry walls. *Acta Mech.* **2011**, *221*, 65–77. [CrossRef]
12. Abdulla, K.; Cunningham, L.S.; Gillie, M. Simulating masonry wall behaviour using a simplified micro-model approach. *Eng. Struct.* **2017**, *151*, 349–365. [CrossRef]
13. Bracchi, S.; Penna, A. A novel macroelement model for the nonlinear analysis of masonry buildings. Part 2: Shear behavior. *Earthq. Eng. Struct. Dyn.* **2021**, *50*, 2212–2232. [CrossRef]
14. Bracchi, S.; Galasco, A.; Penna, A. A novel macroelement model for the nonlinear analysis of masonry buildings. Part 1: Axial and flexural behavior. *Earthq. Eng. Struct. Dyn.* **2021**, *50*, 2233–2252. [CrossRef]
15. Vanin, F.; Penna, A.; Beyer, K. A three-dimensional macroelement for modeling the in-plane and out-of-plane response of masonry walls. *Earthq. Eng. Struct. Dyn.* **2020**, *49*, 1365–1387. [CrossRef]
16. Pantò, B.; Cannizzaro FCaliò, I.; Lourenço, P.B. Numerical and experimental validation of a 3Dmacro-model for the in-plane and out-of-plane behaviour of unreinforced masonry walls. *Int. J. Arch. Herit.* **2017**, *11*, 946–964.
17. Rinaldin, G.; Amadio, C.; Macorini, L. A macro-model with nonlinear springs for seismic analysis of URM buildings. *Earthq. Eng. Struct. Dyn.* **2016**, *45*, 2261–2281. [CrossRef]
18. Lagomarsino, S.; Cattari, S.; Angiolilli, M.; Bracchi, S.; Rota, M.; Penna, A. Modeling and seismic response analysis of existing URM structures. Part 2: Historical buildings. *J. Earthq. Eng.* **2022**, *27*, 1849–1874. [CrossRef]
19. Lagomarsino, S.; Cattari, S. Seismic performance of historical masonry structures through pushover and nonlinear dynamic analyses. In *Perspectives on European Earthquake Engineering and Seismology*; Ansal, A., Ed.; Springer: Cham, Switzerland, 2015; pp. 265–292.
20. Osmanovic, N.; Medic, S.; Hrasnica, M. Seismic Assessment of Existing Masonry Building. In *International Symposium on Innovative and Interdisciplinary Applications of Advanced Technology (IAT), Jahorina, Bosnia and Hercegovina*; Springer: Berlin/Heidelberg, Germany, 2018.
21. Kheyroddin, A.; Saghafi, M.H.; Safakhah, S. Strengthening of Historical Masonry Buildings with Fiber Reinforced Polymers (FRP). In Proceedings of the 7th International Conference on Structural Analysis of Historic Constructions, Shanghai, China, 6–8 October 2010.
22. Bocca, P.; Valente, S.; Grazzini, A.; Alberto, A. Detachment Analysis of Dehumidified Repair Mortars Applied to Historical Masonry Walls. *Int. J. Arch. Herit.* **2014**, *8*, 336–348. [CrossRef]
23. Peng, W.; Long, Z.; Chen, L. Experimental Investigation on the Performance of Historical Squat Masonry Walls Strengthened by UHPC and Reinforced Polymer Mortar Layers. *Appl. Sci.* **2019**, *9*, 2096. [CrossRef]
24. Chen, Z.; Chen, W.; Mai, C.; Shi, J.; Xie, Y.; Hu, H. Experimental Study on the Compressive Behaviors of Brick Masonry Strengthened with Modified Oyster Shell Ash Mortar. *Buildings* **2021**, *11*, 266. [CrossRef]
25. Le, H.H.; Terrade, B.; Garnier, D. Assessing the Three-Dimensional Behaviour of Dry Stone Retaining Walls by Full-Scale Experiments. *Int. J. Arch. Herit.* **2020**, *14*, 1373–1383. [CrossRef]
26. Colas, A.S.; Morel, J.C.; Garnier, D. Assessing the two-dimensional behaviour of drystone retaining walls by full-scale experiments and yield design simulation. *Geotechnique* **2013**, *63*, 107–117. [CrossRef]
27. Munoz, H.; Kiyota, T. Deformation and localisation behaviours of reinforced gravelly backfill using shaking table tests. *J. Rock Mech. Geotech. Eng.* **2020**, *12*, 102–111. [CrossRef]
28. Kazimierowicz-Frankowska, K.; Kulczykowski, M. Laboratory Testing and Theoretical Modeling of Deformations of Reinforced Soil Wall. *Appl. Sci.* **2022**, *12*, 6895. [CrossRef]
29. Liu, Y.; Yao, Z.; Shao, M.; Liu, H.; Zhao, Y. Mechanical Behavior of the Reinforced Retaining Wall under Vehicle Load. *Math. Probl. Eng.* **2021**, *2021*, 2197572. [CrossRef]
30. Quezada, J.C.; Vincens, E.; Mouterde, R.; Morel, J.C. 3D failure of a scale-down dry stone retaining wall: A DEM modeling. *Eng. Struct.* **2016**, *117*, 506–517. [CrossRef]
31. Geng, M. A Short Review on the Dynamic Characteristics of Geogrid-Reinforced Soil Retaining Walls under Cyclic Loading. *Adv. Mater. Sci. Eng.* **2021**, *2021*, 5537912. [CrossRef]

32. Xie, Y. Mechanical Behavior of Rice Glue and Failure Mechanism of Ancient Seawall. Master's Thesis, Zhejiang University, Hangzhou, China, 2013.
33. Feng, S.; Wang, X.; Sun, H.; Zhang, Y.; Li, L. A better understanding of long-range temporal dependence of traffic flow time series. *Phys. A Stat. Mech. Appl.* **2018**, *492*, 639–650. [CrossRef]
34. Dimitriadis, P.; Koutsoyiannis, D.; Iliopoulou, T.; Papanicolaou, P. A global-scale investigation of stochastic similarities in marginal distribution and dependence structure of key hydrological-cycle processes. *Hydrology* **2021**, *8*, 59. [CrossRef]

Disclaimer/Publisher's Note: The statements, opinions and data contained in all publications are solely those of the individual author(s) and contributor(s) and not of MDPI and/or the editor(s). MDPI and/or the editor(s) disclaim responsibility for any injury to people or property resulting from any ideas, methods, instructions or products referred to in the content.